Supplementary Materials for

Decades-Long Changes of the Interstellar Wind Through Our Solar System

P. C. Frisch,* M. Bzowski, G. Livadiotis, D. J. McComas, E. Moebius, H.-R. Mueller, W. R. Pryor, N. A. Schwadron, J. M. Sokół, J. V. Vallerga, J. M. Ajello

*Corresponding author. E-mail: frisch@oddjob.uchicago.edu

Published 6 September 2013, *Science* **341**, 1080 (2013)
DOI: 10.1126/science.1239925

This PDF file includes:

Supplementary Material

Supplementary material — S1

The He^{o} distribution and relation to solar radiation

Comparisons between diverse helium measurements from the inner heliosphere are based on helium trajectory models. In the interstellar medium away from the influence of the heliosphere, He^{o} velocities are generally assumed to be Maxwellian centered around the bulk flow velocity, $V_{\rm bulk}$. The cloud temperature superimposes a randomly oriented velocity of 5.8 $\rm km\ s^{-1}$ on the bulk cloud velocity because the Local Interstellar Cloud (LIC) is warm, with a temperature of $T_{\rm LIC}= 6300 \pm 390$ K found by in situ measurements *(2,8)*. Neutral He^{o} atoms traverse the heliosheath regions relatively undisturbed, and follow Keplerian hyperbolic orbits to the inner heliosphere. Photoionization and electron impact ionization dominate He^{o} destruction within several AU of the Sun *(3,4)*. Drag forces from short-range interactions with the solar wind plasma contribute minor heating of the He^{o} gas that is more apparent in the downwind direction (*21, 22*). A characteristic property of the He^{o} flow through the heliosphere is that particle trajectories depend on both temperature $T_{\rm LIC}$ and bulk velocity $V_{\rm bulk}$ (*23*). The opening angle of the He^{o} focusing cone, and the observed angular spread of He^{o} beam, depends on the ratio $T_{\rm LIC}/{V_{\rm bulk}}^2$ *(2,4)*. Fig. S1 shows the density distribution of interstellar He^{o} in the heliosphere, normalized to the density at infinity (*24*). An upwind neutral particle deficit appears where gravitationally accelerated particles approaching close to the Sun become ionized and seed the formation of the upwind pickup ion crescent. Fig. S1 also shows the IBEX He^{o} observing geometry *(3)*, the highly inclined Ulysses orbit projected onto the ecliptic plane *(8)*, the SOLRAD 11B observing geometry for February 1977 *(12)*, and the interval of the sky observed by Mariner 10 during roll control maneuver seven (RCM7) *(10,11)*.

Photoionization rates of He^{o} by solar extreme ultraviolet (EUV) are important for modeling the survival of He^{o} atoms to the inner heliosphere. Comparisons between the absolute helium ionization rate determined from measurements by the Solar and Heliospheric Observatory (SOHO) and the solar MgII index has shown that the MgII index is an excellent proxy for the ionization rate of He^{o} (*25*). An equally good proxy for the photoionization rate of He is the solar 10.7 cm radio flux, measured daily since 1948. Most of the early studies assumed constant photoionization rates however the solar MgII index is available since 1978. Outside of 1 AU the rapid cooling of solar wind electrons diminishes the importance of electron impact ionization. At 1 AU, the ratio of the polar to equatorial electron impact ionization rates is ~ 0.85 (*25*). This anisotropy in electron impact ionization rates affects the symmetry of the focusing cone during solar minimum conditions. During solar maximum conditions, the total rate appears to be a factor of 2.5 larger than

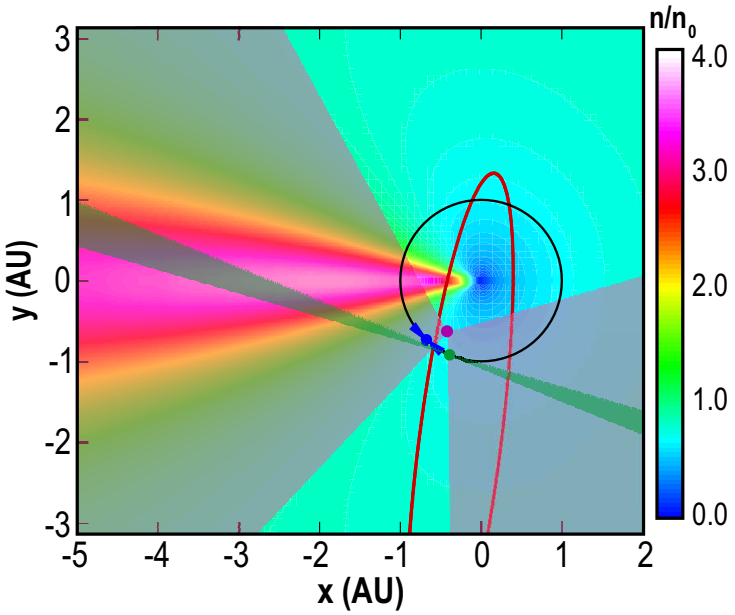

Figure S1: Interstellar helium density in the inner heliosphere. A model of the He^{o} density in the inner heliosphere (*24*) is displayed. The intersection of the ecliptic plane with regions observed by IBEX *(3)*, Mariner 10 during the roll control maneuver RCM7 *(11)* and the February 1977 measurements by SOLRAD 11B *(12)* are indicated. The regions observed by these spacecraft are defined, repectively, by the narrow blue compact double-cone at 1 AU, the narrow extended double-cone centered at 1 AU, and the broad double-cone centered near 0.4 AU. The color-coded density distribution of interstellar He^{o}, relative to the density at infinity, is shown for a two-dimensional slice through the symmetry axis of the focusing cone (*24*). The upwind direction is placed along the positive x-axis to the figure-right, and at y=0. Atoms on both direct and indirect orbits, where atoms have already passed perihelion, contribute to the density downwind of the Sun (toward the left). Interstellar atoms are rapidly ionized inside of 1 AU in the upwind direction (dark blue region), enhancing the upwind pickup densities that create the crescent feature. The partial ellipse shows the projection onto the ecliptic plane of the highly inclined orbit of Ulysses.

during solar minimum conditions, leading to measurable decreases in the fluxes of the 584Å interplanetary glow. Electron impact ionization contributes $\sim 20\%$ of the ionization at 1 AU, and charge-exchange with the solar wind protons less than 4% *(4)*.

Measurements of the He^{o} wind using 584Å emission data are more sensitive to the solar activity cycle than in situ measurements. The 584Å emission forms over long sightlines that are dominated by regions closest to the Sun due to the $1/R^2$ dependence of the illumination, but the entire spatial distribution of the fluorescence and He^{o} atoms must be modeled. The 584Å emission strength depends on the intensity of the solar He^{o} 584Å emission, which is characterized by a Gaussian-like profile with a Doppler width, $\delta\lambda_{dop}$ (where intensity falls to 1/e of the maximum value). Data from the Solar Ultraviolet Measurements of Emitted Radiation (SUMER) instrument on SOHO acquired during 1996–2001 indicate that 80% of the solar profiles have a Doppler width of $\delta\lambda_{dop}$=36.5 ± 1.7 km s^{-1} (*25*). The remaining 10% of the widest, and 10% of the narrowest, profiles had Doppler widths corresponding to 49.5 km s^{-1} and 27.7 km s^{-1} respectively. The solar 584Å emissivity tightly correlates with the solar activity MgII index, and the constancy of $\delta\lambda_{dop}$ over a five-year period suggest that $\delta\lambda_{dop}$ is not related to the solar activity level (*25*).

Related to this effect is the Doppler dimming of the 584Å emission feature, which must be taken into account in models of the 584Å emission distribution. Doppler dimming occurs when the radial component (with respect to the Sun) of the particle velocity is shifted out of the intensity maximum of the solar 584Å line. The Doppler effect introduces an angular dependence on the scattered 584Å emission that depends on the width of the solar emission line. The focusing cone models (*24*) in Fig. S1 show that the absolute value of the radial velocities diminishes/increases for direct/indirect particles in sidewind directions, which shifts particle velocities into and out of, respectively, the core of the solar 584Å emission line. Upwind atoms are gravitationally accelerated into the wings of the solar line. The sidewind decrease in radial velocities leads to enhanced 584Å emission, and the upwind increase in radial velocities

The axis of symmetry of the helium focusing cone provides the direction of the interstellar helium flow and the interstellar wind direction. Table S1 lists the measurements of this wind direction based on 584Å resonant fluorescence and in situ measurements, and measurements of the pickup ion (PUI) focusing cone and upwind crescent.

Supplementary material — S2

Measurements of the He^{o} flow using backscattered 584Å data

Weller and Meier mapped the 584Å resonant scattering from three spacecraft,

and reported independent measurements for the He^{o} flow direction from data acquired on STP 72-1 *(9)* and SOLRAD 11B *(12)*. The first of these measurements, from STP 72-1, looked down the Earth's night cone during the October–January interval and the sightline crossed the focusing cone. Uncertainties of $\pm 3^{\circ}$ were quoted for the entire flow direction, but we use those uncertainties for the longitude alone. With the benefit of the full hot model that described the gravitational forces and effects of Doppler dimming on an interstellar helium gas with a finite temperature, and Orbiting Geophysical Observatory (OSO) 8 results that established the degeneracy of velocity and temperature obtained from hot models, SOLRAD 11B 584Å data obtained a new direction for the interstellar He^{o} flow direction that differed from the STP 72-1 value by 3°. This difference is conservatively adopted as the uncertainty on the SOLRAD 11B longitude, although the difference occurs in the latitude (Table S1). The SOLRAD 11B data were acquired during 1976.9–1977.1 from locations around the focusing cone. Solar photoionization rates assumed for the SOLRAD 11B observations ranged from 6.8×10^{-8} sec^{-1} to 1.3×10^{-7} sec^{-1}. The first rate agrees with predictions of the Bzowski et al. (*26*) historical solar radiation model, while the second rate is a factor of two larger than the expected rates. The 584Å emissivity was assumed to vary by less than 10%, based on 10.7 cm proxy. Electron impact ionization of He^{o} atoms was not included in the early models, but would have little effect on the flow direction if the ionization rates are symmetric around the focusing cone. A reasonable Doppler width of 36.3 $\mathrm{km\ s^{-1}}$ was assumed for the solar 584Å line, consistent with the later SUMER data.

Inaccurate ionization rates should not distort the flow longitude obtained from 584Å data if the focusing cone is axisymmetric. Such uncertainties can lead to misplacements in modeled locations of scattering atoms in the sense that rates above the true values implicitly place the source at larger distances, so that the observed width of the observed focusing cone becomes associated in the model with either low temperatures or larger velocities because of the angular dependence of trajectories on T/V^2.

Observations of resonant He^{o} 584Å scattering were acquired by the interplanetary mission Mariner 10 during the short ($\leq$4-hour) RCM7 and roll control maneuver three (RCM3) enroute to Venus *(10,11)*. These data are available online at the IBEX project web site http://ibex.swri.edu/researchers/publicdata.shtml. The RCM7 data were analyzed using a modified cold model, that included a reasonable approximation for the photoionization rate according to the historical rates (*26*), estimates for electron impact ionization, and approximations for the thermal characteristics of the gas. The RCM7 scan passed within 0.6 AU of the Sun, where electron impact ionization is significant. Mariner 10 simultaneously measured the interstellar wind resonant Lyα fluorescence from H^{o}. The RCM7 flow direction was obtained from fits to the downwind 584Å maximum and Lyα minimum fluxes

(11), and confirmed by tests with RCM3 He^{o} data *(12)*. RCM3 data provided the best sensitivity to the focusing cone symmetry because the maneuver occurred when the spacecraft was close to the downwind axis of the focusing cone. Models of the RCM3 He^{o} 584Å data found that agreement with the data was significantly degraded if the flow direction differed by more than 5° from λ,β= $73.4°, -5.4°$ *(11)*. The combined RCM7 and RCM3 data give an ecliptic longitude of the flow direction from Mariner 10 data of λ=$73.4° \pm 5°$.

A key question is whether the modeling of early 584Å data was capable of discriminating between the ecliptic longitudes of the flow reported by IBEX versus the original flow direction obtained from Mariner 10 data and listed in Table S1. We have tested this possibility by evaluating the RCM7 He^{o} data for different possible flow longitudes using the original models of *(10)*. We find that the RMS differences between the model and RCM7 data are 16.18%, 13.25%, 10.65%, 10.69%, and 11.43% for ecliptic flow longitudes of 89°, 84°, 79°, 74°, and 69° respectively. The RCM7 data fit the Ulysses and IBEX directions equally well, with an RMS deviation between the models and data of 10.7%, but are inconsistent with larger or smaller directions. Since the RCM3 data provided the best sensitivity to the He^{o} wind axis *(11)*, we consider the longitude of the He^{o} flow and uncertainties of ± 5 to be fairly stated for the Mariner 10 data in Table S1.

While in a survey mode in 1992-1993, the Extreme Ultraviolet Explorer (EUVE) observed sightlines along anti-Sun directions down the night-shadow. These data provided a uniform set of 584Å emission data that traced the excess flux levels in the focusing cone (Fig. 2 in *(14)*). These data were analyzed with contemporary models of the He^{o} distribution in the heliosphere that included electron impact ionization and removed short term variations in the solar 584Å flux using the solar MgII index as a proxy. The ecliptic longitude of the He^{o} flow was determined from the proxy-corrected data and a Gaussian fit to the brightness of the 584Å emissivity as the instrument slit swept across the focusing cone. The longitude of the flow direction was quoted to high accuracy, $74.7° \pm 0.5°$. Perusal of the data in Fig. 2 of *(14)* indicates that the peak flux actually occurred longward of the quoted longitude for the focusing cone, followed by a dropout of data between approximate longitudes 78.3°–81.3°. The Gaussian fit was dominated by the lower intensity wings of the focusing cone emission, and the flux excursions at high flux levels were not understood. The presence of the anomalously high emissivity 2°–3° longwards of the focusing cone peak, and the data dropout at slightly larger longitudes, makes it difficult to relate the focusing cone wings (where the brightening effect of the Doppler shift is largest) with the peak of the cone that defines the He^{o} wind direction. The uncertainty estimates of $\pm 0.5°$ quoted in the original publication *(14)* may be underestimated.

Prognoz 6 was launched into a highly eccentric orbit in 1977, where photometers sensitive to the He^{o} 584Å emission acquired data over a period of 1.5 months that included a traversal of the gravitational focusing cone. These data were analyzed in two ways to obtain the axis of the focusing cone, based on the geometry of the fluxes determined from two instrument channels, and based on a modified hot model constructed by summing over a set of models calculated with individual Boltzman-Maxwell velocity distributions in interstellar space *(13)*. The two values (Table S1) differ by 3.2°, with the geometric value best matching the earlier 1970's directions and the modeled value best matching the EUVE results. Both values are included as separate data points in Fig. 1. A later reanalysis of these data, for the goal of reconciling the Prognoz 6 He^{o} flow direction to the Ulysses direction, found that the Prognoz 6 and Ulysses directions agreed (*27*). Since the reanalysis was designed to show whether or not the Prognoz 6 data could be made compatible with the interstellar wind data collected during the 1990s, the study did not qualify as an independent result and was not included in our analysis.

Additional measurements of the He^{o} flow direction were made by NOZOMI in 2000-2001 from a Mars transfer orbit (perihelion 1 AU, aphelion 1.5 AU) (*20*). Maximum fluxes were observed from the focusing cone. The data were interpreted with a hot model that did not include electron impact ionization. The model assumed the velocity and gas temperature from the Ulysses results, and left the cone axis as the only free parameter in the simulations. The interpretation of the data did not include corrections for the small-scale periodicities of the illuminating solar 584Å radiation field (e.g. Fig. 2 in *(14)*) that are expected under solar-maximum conditions. The flow direction found from the NOZOMI data is consistent with the IBEX value.

Supplementary material — S3

Dust and Hydrogen in the Interstellar Wind

Values for the interstellar wind direction that are based on mechanisms involving uncertain trajectories through the heliosphere or a poorly defined contribution from outer heliosphere processes are not included in this study. Measurements of the HI Lyα fluorescence signal fall in this category, as do in situ detections of interstellar dust. The H^{o} trajectories vary with the ratio of radiation pressure to gravitational forces, and radiation pressure varies throughout the twenty year propagation time of H^{o} through the heliosphere. The difference between the upwind direction found from H^{o}, λ,β= $252.5° \pm 0.7°$, $8.9° \pm 0.5°$, versus the He^{o} direction found from the in situ He^{o} measurements (*28*) has been attributed to the production

Table S1: Historical measurements of interstellar wind direction*

Observations (years)	Velocity ($\mathrm{km\ s^{-1}}$)	Downwind direction (λ, β, deg)	Method	Reference
1972.8–1973.6	5–20	73.2 ($\pm$3)†,–7.4	He 584Å	STP 72-1 *(9)*
1974.1–1974.1	[22 ± 3]‡	73.4 ($\pm$5)†,–5.4	He 584Å	Mariner 10 *(10,11)*
1976.9–1977.1	22-28	73.6 ($\pm$3),–4.4	He 584Å	SOLRAD11B *(12)*
1977.7–1978.1	27 ± 3	72.2 ± 3,-7.2 ± 3	He 584Å	Prognoz 6-A *(13)*
1977.7–1978.1	27 ± 3	75.2 ± 3,-6.0 ± 3	He 584Å	Prognoz 6-B *(13)*
1990.9–1991.6	26.2 ± 0.6	$73.8\ \pm 2.2$,$-5.2\ \pm 0.6$	He in situ	Ulysses *(8)*
1992.6–1993.6	24.5 ± 2.0	74.7 ± 0.5,-5.7 ± 0.5	He 584Å	EUVE *(14)*
1994.9–1996.5	26.3 ± 0.4	$75.4\ \pm 0.4$,$-5.2\ \pm 0.2$	He in situ	Ulysses *(8)*
1997.3–2002.0	...	$74.4\ \pm 0.3$ (...)	He PUI	ACE *(15)*
2000–2001	...	78.7 ± 3.4,3.5	He 584Å	Nozomi (*20*)
2000.8–2002.6	26.3 ± 0.4	$75.4\ \pm 0.5$,$-5.2\ \pm 0.2$	He in situ	Ulysses *(8)*
2007.3–2009.2	...	$76.0\ \pm 6.0$	He PUI cone	MESSENGER*(17)*
2007.3–2009.2	...	$77.0\ \pm 1.5$	He PUI cone	ACE *(17)*
2007.3–2011.3	...	78.9 ± 3.1	O PUI cres.	STEREO A *(16)*
2007.3–2011.3	...	77.4 ± 1.9	He PUI cone	STEREO A *(16)*
2007.3–2011.3	...	77.4 ± 5.0	Ne PUI cone	STEREO A *(16)*
2007.3–2011.3	...	80.4 ± 5.4	He PUI cres.	STEREO A *(16)*
2007.3–2011.3	...	79.7 ± 2.6	Ne PUI cres.	STEREO A *(16)*
2009.2–2011.2	22.3 ± 0.4	$79.0^{+3.0}_{-3.5}$§,-5.0 ± 0.2	He in situ	IBEX *(2)*

*All directions are presented in the J2000 epoch. The acronym PUI stands for pickup ions, and "cres." stands for crescent. The PUI data do not give the latitude of the He flow. For the Prognoz 6 data, A and B stand for the geometric and He trajectory models, respectively. †These uncertainties were originally quoted for the combined flow longitude and latitude, and are applied here to the longitude only. ‡These models used the Copernicus velocity for interstellar H^{o} inside of the heliosphere (see references in *(10)*). §This He flow direction is further constrained to be $80.0^{+2.0}_{-1.0}$ degrees by restricting the longitude range using the independent LIC temperature obtained from Sirius data (SM-S4) combined with the longitude parameter range shown in Fig. 1 of *(2)*. The temperature constraints are used for modeling the flow temporal variations.

of H^o secondaries by charge exchange with protons from the magnetically deflected plasma flow in the heliosheath regions.

The direction of interstellar dust flowing through the heliosphere (*30*) agrees with the interstellar wind direction obtained from IBEX measurements of interstellar He^o *(2)*. Approximately 0.6% of the mass of the LIC is contained in dust grains that have small enough charge-to-mass ratios to be able to penetrate the heliosheath plasmas and enter the heliosphere *(1)*. The interstellar wind direction has been determined from Ulysses and Galileo in situ measurements of interstellar dust. Ulysses provided data on interstellar dust outside of the ecliptic plane where there is minimal confusion with zodiacal dust. The upwind direction for the dust flow through the heliosphere obtained from dust grain measurements from Ulysses and Galileo prior to 1998 is toward λ,β= $259^\circ \pm 20^\circ$, $8^\circ \pm 10^\circ$ (*29, 30*). The solar cycle minimum during the 1990's corresponded to a solar magnetic polarity that defocused grains with large charge-to-mass ratios away from the ecliptic plane, and undeflected large grains formed the basis of this measurement of the interstellar dust wind. In situ Ulysses measurements of the interstellar dust angular distribution yield an interstellar dust velocity before 2000 of 24.5 ± 1.2 km s^{-1} (*31*). The dust velocity vector traced by Ulysses and Galileo during the decade of the 1990's agrees with the interstellar wind velocity determined from the in situ He^o measurements, although the uncertainties on the dust measurements are larger. The impact of interstellar dust on the STEREO spacecraft create waves measured by plasma detectors. The direction of the flow of interstellar dust through the heliosphere determined for STEREO data collected during the years 2007–2011 is $259.8^\circ \pm 2.5^\circ$ (*32*). This direction agrees with the less precise measurement of the interstellar dust direction found from Ulysses and Galileo data that were collected during the conditions of the opposite solar cycle magnetic polarity in the 1990s.

The dust result is not included in the evaluation of variations in wind direction because these submicron-sized charged grains are highly sensitive to the heliosphere plasma and radiation environment *(1)*. Ulysses measured a 30° southward shift of the upwind direction of the interstellar dust wind in 2005 (*33*). This shift is likely to have been the response of charged dust grains to the solar magnetic activity cycle.

Supplementary material — S4

LIC temperature and turbulence toward Sirius

Because of the degeneracy between temperature and velocity for the trajectory of an interstellar He^{o} atoms through the heliosphere (*23*), independent information on the LIC temperature improves determinations of the most likely interstellar He^{o} wind direction. An alternate source of information on the temperature of the LIC surrounding the heliosphere is provided by interstellar absorption lines formed in the Local Interstellar Cloud (LIC) that are Doppler broadened by the thermal motions of atoms. An additional non-thermal broadening of the line is interpreted as turbulence. The nearest star showing LIC absorption lines is Sirius (α CMa, 2.7 pc (*34*)) and the broadening of LIC absorption lines toward Sirius provides an independent measure of the LIC temperature. For an H^{o} density of 0.2 cm^{-3} and column density of N(H^{o} $= 4.0 \times 10^{17}$ cm^{-2}, the length of the LIC toward Sirius is about 0.6 pc *(1)*. Photoionization models of this sightline indicate that in the direction of Sirius, the LIC temperature varies by less than 5% (*35*) between the cloud edge and the Sun. The Doppler broadening of an absorption line is given by $b_{\rm dop}^2 = (2kT/m)^2 + \xi^2$, where T is the temperature, ξ is turbulence, m is the particle mass, and k is the Boltzmann constant. The turbulent velocity derived from absorption line widths represents turbulence in gas velocities that areprojected onto the radial line of sight.

The Doppler widths of interstellar Ca^{+} (1.6 ± 0.7 km s^{-1} (*36*)), and Fe^{+} and Mg^{+} (*37*) span a mass range of 2.3 and provide a valid means for an independent estimate of the LIC temperature. Fig. S2 shows the temperature-ξ parameter space spanned by the broadening of the LIC optical Ca^{+} line, and the Fe^{+}, and Mg^{+} ultraviolet lines toward Sirius. The intersection of the allowed range for each species, Fe^{+}, Mg^{+}, and Ca^{+}, shows the temperature-turbulence solution that is consistent with all of the measurements (black region in Fig. S2). These data indicate a median LIC temperature of 5800^{+300}_{-700} K, with corresponding turbulence of 1.66 ± 0.12 km s^{-1}. The Sirius LIC temperature is at the lower end of the range determined from the IBEX parameter region. Converting this temperature to a longitude range using Fig. 1 in McComas et al. *(2)* constrains the flow longitude of the LIC to $80.0^{+2.0}_{-1.0}$ degrees. The LIC temperature from Sirius data is not consistent with the large value that is needed to bring the IBEX and Ulysses flow longitudes into agreement according to the allowed parameter space in Fig. 1 in *(2)*.

The derivations of helium temperatures from recent heliospheric measurements, 1990 and later, have benefited from a better understanding of particle ionization than the earliest data, so we look only at LIC temperature data acquired since 1990. The full parameter space for the IBEX wind direction *(2)* is listed in Table S1. If

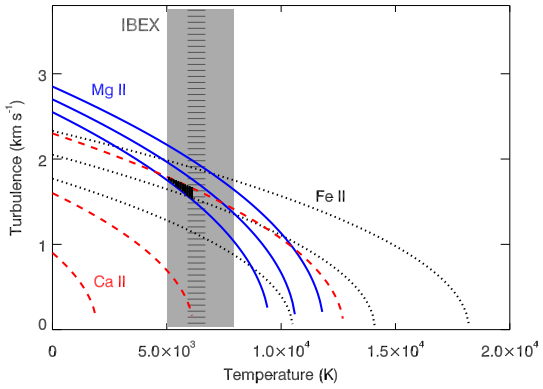

Figure S2: Parameter space for LIC temperature and turbulence toward Sirius. Constraints on the temperature and turbulence are shown based on absorption lines measured in the optical (Ca^+, red dashed lines), and ultraviolet (Mg^+, blue lines, and Fe^+,black dotted line) toward Sirius. The widths of the absorption lines in velocity space are assumed to consist of a non-thermal mass-independent turbulent component superimposed on the main thermal distribution. The gray-shaded box shows the bounding range on the LIC temperature from IBEX He^o data, and the vertical stripe gives the most probable temperature *(2)*. The phase space area that is consistent with all data (small black speckled region) gives a median LIC temperature of 5800^{+300}_{-700} K toward Sirius (SM-S4).

only the most probable values are considered, the LIC direction and temperature obtained from the IBEX data are $\lambda = 79.00^\circ \pm 0.47^\circ,\ \beta = -4.98^\circ \pm 0.21^\circ$) and $\mathrm{T} = 6300^\circ \pm 390^\circ$ K *(2)*. EUVE observations during 1992.6–1993.6 yielded a best fit LIC temperature of $6000^\circ \pm 1500^\circ$ K *(14)*. The best temperature from the Ulysses data, representing observations collected over three period of time during 1990.9 2002.6, is 6300 ± 340 K *(8)*. The three individual periods of Ulysses measurements going into this value were during 1990.86–1991.6, and the two fast-latitude scans during 1994.85–1996.5 and 2000.8–2002.6. Temperatures of 8150 ± 960 K, 6305 ± 340 K, and 6466 ± 400 K were reported, respectively, for these individual periods of times *(8)*. The mean LIC temperature obtained from these three sets of data, the EUVE 584Å data, the Ulysses best-fit value, and the most probable IBEX temperature, is 6644 ± 718 K. Thus a fairly consistent picture of a warm LIC temperature at the heliosphere boundaries emerges from observations conducted within the heliosphere.

This LIC temperature derived from the interstellar absorption line data (Fig. S2) is consistent with the mean LIC temperature of the best fits to heliosphere data that is listed above, e.g. 5799^{+300}_{-700} K compared to $6644^\circ \pm 718^\circ$ K, and is used in Table S1 to constrain the IBEX longitude parameter space shown in Fig. 1 of *(2)*.

Our LIC temperature does not agree with the higher LIC temperature derived by Hebrard et al. (*34*) from simultaneous fits of nineteen absorption lines that included heavily saturated lines, lines from entirely neutral species, and data with a significantly lower signal-to-noise ratio than the Fe^+ and Mg^+ data used here. Our analysis is restricted to ions of Fe^+, Mg^+, and Ca^+, which have similar depletion patterns (where atoms missing from the gas collect on interstellar dust grains) and trace both ionized and neutral gas. Heavily saturated absorption lines can sample lower column density gases that are invisible to unsaturated or weak absorption lines. There is no reason to assume that the kinetic turbulence has a constant value throughout the LIC since the LIC is part of an interstellar gas flow that is decelerating *(1)*. It is possible that the difference between temperature values obtained from elements with similar behaviors in the interstellar medium, versus saturated lines that pick up the wings of the velocity distributions, is due to variations in the kinetic turbulence throughout the cloud.

Supplementary material — S5

Statistical analysis of helium flow data

The result that the He^o flow longitude has increased over the past several decades is established by statistical tests. For the first statistical test, the null hypothesis (H_0) is that the helium flow direction has a constant ecliptic longitude λ, i.e., its values are time invariant. This is tested by examining the chi-square value of fit-

ting a constant ecliptic longitude along the given data points. In general the fitting between a given dataset $\{\lambda_i\}_{i=1}^N$, where λ_i is the flow longitude, and the statistical model $\{V(t_i;p)\}_{i=1}^N$, involves finding the optimal parameter value $p = p^*$ that minimizes the total square deviations between model and data. In our case, the fitting involves minimizing the chi-square $\chi^2(p) = \sum_{i=1}^N \sigma_{\lambda_i}^{-2}(\lambda_i - p)^2$, with $\lambda_i \pm \sigma_{\lambda_i}$ given in Table S1, for $i = 1, ..., N$, with $N = 19$, while the statistical model used here is simply given by a fixed parameter value, $V(t;p) = p$. The result is the mean value $p^* = \sum_{i=1}^N w_i\lambda_i$ with variance $\sigma_p^2 = \frac{1}{N-1}\sum_{i=1}^N w_i(\lambda_i - p^*)^2$, where $w_i = \sigma_{\lambda_i}^{-2}/\sum_{j=1}^N \sigma_{\lambda_j}^{-2}$. The total error of the fitting parameter is given by two independent errors, (i) the statistical error, given by the standard deviation $\delta p_{st}^* = \sigma_p$, and (ii) the propagation error, δp_{pr}^*, which results from the propagation of the errors of each of the measurements $\{\lambda_i \pm \sigma_{\lambda_i}\}_{i=1}^N$. Note that the average p^* is a function of $\{\lambda_i\}_{i=1}^N$ with errors $\{\sigma_{\lambda_i}\}_{i=1}^N$ that propagate according to $\delta p_{pr}^* = \sqrt{\sum_{i=1}^N (\frac{\partial p^*}{\partial \lambda_i})^2 \sigma_{\lambda_i}^2} = \ldots = 1/\sum_{i=1}^N \sigma_{\lambda_i}^{-2}$. The total error is $\delta p^* = \sqrt{{\delta p_{st}^*}^2 + {\delta p_{pr}^*}^2}$. Finally, the estimated chi-square value that characterizes the fitting is $\chi_{est}^2 = \sum_{i=1}^N \sigma_{\lambda_i}^{-2}(\lambda_i - p^*)^2$, and its reduced value is $\chi_{red}^2 = \frac{1}{M}\chi_{est}^2$ with $M = N - 1$ degrees of freedom.

The next null hypothesis that will be tested is the simple model that the helium flow direction has an ecliptic longitude λ that varies linearly with time. This is tested by examining the chi-square value when fitting the bi-parametric linear statistical model $V(t;p_1,p_2) = p_1 + p_2 \cdot t$ to the given data points. Therefore, we minimize the chi-square $\chi^2(p_1,p_2) = \sum_{i=1}^N \sigma_i(p_2)^{-2}(\lambda_i - p_1 - p_2 \cdot t_i)^2$, where the total variance that characterize each data point is now given by $\sigma_i(p_2)^2 = \sigma_{\lambda_i}^2 + p_2^2 \cdot \sigma_{t_i}^2$ (*38*). Note that the standard weighting involved in χ^2 typically uses the variance of the data to-be-fitted, i.e., $\sigma_{\lambda_i}^2$. However, this χ^2-weighting is a good approximation, only if the model $\{V(t_i;p_1,p_2)\}_{i=1}^N$ does not include significant errors, i.e., if the errors $\sigma_{t_i}^2$ can be ignored (see below for this case). The time "errors" are defined by the endpoints of the observation dates (given in Table S1) and they are significant for the statistical analysis. The global minimum of chi-square gives the optimal parameter values, (p_1^*, p_2^*), by solving the two equations $\frac{\partial \chi^2(p_1,p_2)}{\partial p_k} = 0$, for $k = 1, 2$. The statistical errors of these values are given by $\delta {p_k}_{st}^* = \sqrt{\chi_{red}^2 \cdot H_{kk}^{-1}}$, $k = 1, 2$, where H is the Hessian matrix of the chi-square at the global minimum, and H_{kk}^{-1} is the k^{th} diagonal element of its inverse matrix (*39*); the estimated chi-square value is $\chi_{est}^2 = \sum_{i=1}^N \sigma_i(p_2^*)^{-2}(\lambda_i - p_1^* - p_2^* \cdot t_i)^2$, and its reduced value is $\chi_{red}^2 = \frac{1}{M}\chi_{est}^2$ with $M = N - 2$ degrees of freedom. The propagation errors of the measurements $\{t_i \pm \sigma_{t_i}, \lambda_i \pm \sigma_{\lambda_i}\}_{i=1}^N$ are given by $\delta {p_k}_{pr}^* = \sqrt{\sum_{i=1}^N [(\frac{\partial {p_k}^*}{\partial t_i})^2 \sigma_{t_i}^2 + (\frac{\partial {p_k}^*}{\partial \lambda_i})^2 \sigma_{\lambda_i}^2]}$, $k = 1, 2$, where the derivatives are numerically derived.

The reduced chi-square value χ_{red}^2 is given by the estimated χ_{est}^2 divided equivalently to all the degrees of freedom M. This has to be $\sim$1 for a good fitting. Fur-

thermore, a better estimation of the goodness is derived from comparing the calculated χ^2_{est} value and the chi-square distribution, $P(\chi^2; M) = \frac{2^{-\frac{M}{2}}}{\Gamma(\frac{M}{2})}(\chi^2)^{\frac{M}{2}-1}\mathrm{e}^{-\frac{1}{2}\chi^2}$, that is the distribution of all the possible χ^2 values. The likelihood of having an χ^2 value equal to or smaller than the estimated value χ^2_{est}, is given by the cumulative distribution $P(0 \leq \chi^2 \leq \chi^2_{est}) = \int_0^{\chi^2_{est}} P(\chi^2; M)d\chi^2$, while the likelihood of having a χ^2 value equal to or larger than the estimated value χ^2_{est}, is given by the complementary cumulative distribution $P(\chi^2_{est} \leq \chi^2 \leq \infty) = \int_{\chi^2_{est}}^{\infty} P(\chi^2; M)d\chi^2$. Therefore, the probability of taking a result χ^2, more extreme than the observed value χ^2_{est}, is given by the p-value that equals the minimum between the two probabilities, $P(0 \leq \chi^2 \leq \chi^2_{est})$ and $P(\chi^2_{est} \leq \chi^2 \leq \infty)$. A null hypothesis associated with p-value smaller than the significance level of ~ 0.05 is typically rejected.

For the first statistical model of constant longitude, we use only the longitude data $\{\lambda_i \pm \sigma_{\lambda_i}\}_{i=1}^N$, with $N = 19$, and find $p^* \pm \delta p^* = 75.1^\circ \pm 1.3^\circ$, $\chi^2_{est} = 30.7$, $\chi^2_{red} = 1.71$, correlation coefficient $r = 55.3\%$, and p-value $= 0.031$ (< 0.05), so H_0 is rejected as unlikely. For the second statistical model of linearly increasing longitude, we use both time and longitude data $\{t_i \pm \sigma_{t_i}, \lambda_i \pm \sigma_{\lambda_i}\}_{i=1}^N$, with $N = 19$, and find $p_1^* \pm \delta p_1^* = 70.6^\circ \pm 1.6^\circ$, $p_2^* \pm \delta p_2^* = 0.17^\circ \pm 0.06^\circ$, $\chi^2_{est} = 16.5$, $\chi^2_{red} = 0.97$, correlation coefficient $r = 65.0\%$, and p-value $= 0.49$ (> 0.05), so H_0 is accepted as highly likely. These two models are plotted in Fig. 1, where the green shaded region shows the uncertainties on the second statistical model corresponding to an upper limit of $p_1^* + \delta p_1^* + (p_2^* + \delta p_2^*) * t_i$ and lower limit of $p_1^* - \delta p_1^* + (p_2^* - \delta p_2^*) * t_i$.

In order to investigate the statistical sensitivity of the above results, the longitude uncertainties are multiplied by a scale factor s, for all data collected prior to 2000 (in case those data have underestimated uncertainties). Fig. S3 shows χ^2_{red} and p-values for both the hypotheses of constant (left column) and linearly increasing longitude (middle column). These results show that for $1.14 < s$, the first statistical model of constant longitude is likely, while for $0.47 < s < 2.67$, the second model of linearly increasing longitude is likely. In the right column of Fig. S3, we observe the ratio of $|\chi^2_{red} - 1|$ values (upper panel) and the ratio of the p-values (lower panel), of the linearly increasing longitude to the constant longitude hypotheses. The ratio of $|\chi^2_{red} - 1|$ is < 1 and the ratio of the p-values is > 1 for $s > 1.77$. Hence, the hypothesis of constant longitude is more likely for $1.77 < s$, while the hypothesis of linearly increasing longitude is more likely for $0.47 < s < 1.77$. Therefore, our results can be characterized as "statistically stable"; namely, the hypotheses of constant and linearly increasing longitude are respectively rejected and accepted, for any variation of the scale of the uncertainties.

In Table S2 we include the results of both the tests for constant and linearly increasing ecliptic longitude. Fig. S3 shows the statistical models.

Uncertainties on the time of observation are included above in the second sta-

Table S2: Test for Constant and Linearly Increasing Helium Ecliptic Longitude

Quantity/Description	**Statistical Models**	
H_0	Constant longitude λ	Linearly increasing longitude λ
Statistical model	$V(t;p) = p$	$V(t;p_1,p_2) = p_1 + p_2 \cdot t$
Data	$\{\lambda_i \pm \sigma_{\lambda_i}\}_{i=1}^{N}$	$\{t_i \pm \sigma_{t_i}, \lambda_i \pm \sigma_{\lambda_i}\}_{i=1}^{N}$
Degrees of freedom (M)	$N - 1 = 18$	$N - 2 = 17$
Optimization values	$p^* \pm \delta p^* = 75.1^\circ \pm 1.3^\circ$	$p_1^* \pm \delta p_1^* = 70.6^\circ \pm 1.6^\circ$, $p_2^* \pm \delta p_2^* = 0.17^\circ \pm 0.06^\circ$
χ_{est}	30.7	16.5
$\chi^2_{red} = \frac{1}{M}\chi^2_{est}$	1.71	0.97
Correlation Coefficient r	55.3%	65.0%
p-value	0.031 (< 0.05)	0.49 (> 0.05)
Test Rating	H_0 is rejected as **Unlikely**	H_0 is accepted as **Highly Likely**

Notes: The used data $\{t_i \pm \sigma_{t_i}, \lambda_i \pm \sigma_{\lambda_i}\}_{i=1}^{N}$ correspond to Table S1, with the IBEX longitude interval specified by the Sirius temperature (SM-S4) constraint applied to Fig. 1 of *(2)*.

tistical model for a linear increase in flow longitude with time, where we have assumed that all uncertainties are normally distributed. For the diverse set of data displayed in Table S1, the window of time over which the measurements were collected does not have a well-defined relation to the true uncertainty in the time of the observation. Therefore the linear fit to the data was repeated by weighting the fits using only the uncertainties on the longitude and ignoring the length of time over which those data were collected. For this fit, shown as the purple short-dash line in Fig. 1, the best-fitting model to the flow longitude is $\lambda(\mathrm{deg}) = 71.7(\pm 1.7) + 0.12(\pm 0.06) * t_{1970}$. Therefore our primary conclusion that the longitude of the interstellar flow through the heliosphere has increased with time is not sensitive to the weighting scheme of a linear fit.

Finally, we remark that more elaborate statistical models of the time dependence, e.g., the parabolic model, $V(t;p_1,p_2,p_3) = p_1 + p_2 \cdot t + p_3 \cdot t^2$, cannot provide an improved fit that matches better these data, because there is not yet a well-established systematic methodology for fitting when all variables are characterized by significant uncertainties. In such a case, where the uncertainties of all variables must be considered, only the fitting method of the bi-parametrical linear model, $V(t;p_1,p_2) = p_1 + p_2 \cdot t$, has been consistently developed (*38*). Given the absence of such a method for any more complex statistical models, we may fit the parabolic model by ignoring the time uncertainties; this gives $V(t) \cong 75.637^\circ - 0.20438^\circ \cdot t + 0.0063948^\circ \cdot t^2$ (a minimum exists for $t = 1986$). However, the construction of the chi-square without taking into account all the errors

$\{t_i \pm \sigma_{t_i}, \lambda_i \pm \sigma_{\lambda_i}\}_{i=1}^{N}$, leads to biased estimations of the involved parameters, and thus, only the constant and linear models are characterized by a reliable fitting.

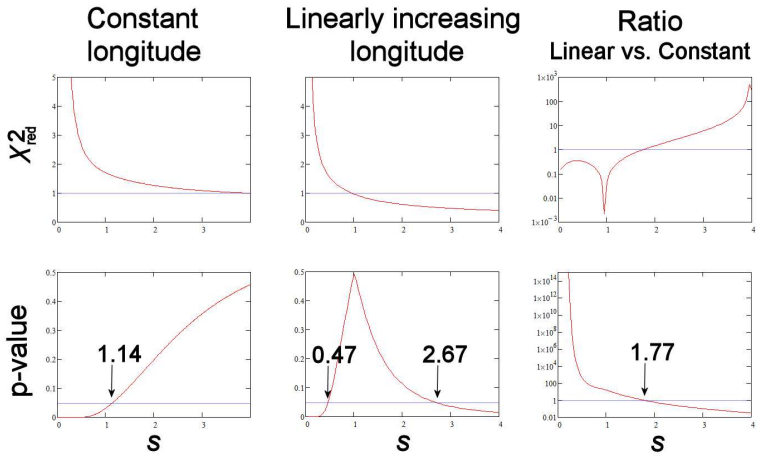

Figure S3: Results of statistical models for constant longitude (left column) and linearly increasing longitude (middle column). The top panels show χ^2_{red} and the bottom panels show the p-values. The ratios of $|\chi^2_{red} - 1|$ and p-values of the second model (linearly increasing longitude) to the first model (constant longitude) are shown in the right column. The critical values of s are shown: $s > 1.14$, where the constant model is likely, $0.47 < s < 2.67$, where the linear model becomes likely, and $s < 1.77$, where the linear model is more likely than the constant model.

References

20. H. Nakagawa, *et al.*, *Astron.&Astrophys.* **491**, 29 (2008).

21. H. J. Fahr, H. U. Nass, D. Rucinski, *Astron.&Astrophys.* **142**, 476 (1985).

22. M. Gruntman, *J. Geophys. Res.(Space Physics)* **doi=10.1002/jgra.50199** (2013).

23. M. A. Lee, *et al.*, *ApJS* **198**, 10 (2012).

24. H.-R. Müller, J. H. Cohen, *Am. Inst. Phy. Conf. Proc.*, J. Heerikhuisen, G. Li, N. Pogorelov, G. Zank, eds. (2012), vol. 1436 of *Am. Inst. Phy. Conf. Proc.*, pp. 233–238.

25. D. R. McMullin, *et al.*, *Astron.&Astrophys.* **426**, 885 (2004).

26. M. Bzowski, *et al.*, *"Cross-Calibration of Past and Present Far UV Spectra of Solar System Objects and the Heliosphere, SSI Scientific Report Series 13"*, M. S. R.M. Bonnet, E. Qumerais, ed. (2013), pp. 67–138.

27. R. Lallement, *et al.*, *Astron.&Astrophys.* **426**, 875 (2004).

28. R. Lallement, *et al.*, *Twelfth International Solar Wind Conference* **58**, 951 (2010).

29. P. C. Frisch, *et al.*, *Space Sci. Rev.* **146**, 235 (2009).

30. P. C. Frisch, *et al.*, *Astrophys. J.* **525**, 492 (1999).

31. H. Kimura, I. Mann, E. K. Jessberger, *Astrophys. J.* **582**, 846 (2003).

32. S. Belheouane, *et al.*, *Sol. Phys.* **281**, 501 (2012).

33. H. Krüger, *et al.*, *Planet. Space Sci.* **58**, 951 (2010).

34. G. Hebrard, *et al.*, *Astron.&Astrophys.* **350**, 643 (1999).

35. J. D. Slavin, P. C. Frisch, *Astrophys. J.* **565**, 364 (2002).

36. P. C. Frisch, L. Grodnicki, D. E. Welty, *Astrophys. J.* **574**, 834 (2002).

37. R. Lallement, P. Bertin, R. Ferlet, A. Vidal-Madjar, J. L. Bertaux, *Astron.&Astrophys.* **286**, 898 (1994).

38. W. E. Deming, *in 'Statistical adjustment of data', New York: Dover* (1964).

39. G. Livadiotis, *Physica A* **375**, 518 (2007).

References

1. P. C. Frisch, S. Redfield, J. Slavin, The interstellar medium surrounding the Sun. *Annu. Rev. Astron. Astrophys.* **49**, 237–279 (2011). doi:10.1146/annurev-astro-081710-102613

2. D. J. McComas, D. Alexashov, M. Bzowski, H. Fahr, J. Heerikhuisen, V. Izmodenov, M. A. Lee, E. Möbius, N. Pogorelov, N. A. Schwadron, G. P. Zank, The heliosphere's interstellar interaction: No bow shock. *Science* **336**, 1291–1293 (2012). doi:10.1126/science.1221054 Medline

3. E. Möbius, P. Bochsler, M. Bzowski, D. Heirtzler, M. A. Kubiak, H. Kucharek, M. A. Lee, T. Leonard, N. A. Schwadron, X. Wu, S. A. Fuselier, G. Crew, D. J. McComas, L. Petersen, L. Saul, D. Valovcin, R. Vanderspek, P. Wurz, Interstellar gas flow parameters derived from Interstellar Boundary Explorer-Lo observations in 2009 and 2010: Analytical analysis. *Astrophys. J. Suppl. Ser*. **198**, 11 (2012). doi:10.1088/0067-0049/198/2/11

4. M. Bzowski, M. A. Kubiak, E. Möbius, P. Bochsler, T. Leonard, D. Heirtzler, H. Kucharek, J. M. Sokół, M. Hłond, G. B. Crew, N. A. Schwadron, S. A. Fuselier, D. J. McComas, Neutral interstellar helium parameters based on IBEX-Lo observations and test particle calculations. *Astrophys. J. Suppl. Ser.* **198**, 12 (2012). doi:10.1088/0067-0049/198/2/12

5. J. W. Armstrong, B. J. Rickett, S. R. Spangler, Electron density power spectrum in the local interstellar medium. *Astrophys. J.* **443**, 209 (1995). doi:10.1086/175515

6. S. R. Spangler, A. H. Savage, S. Redfield, Properties of turbulence in the very local interstellar clouds. *Astrophys. J.* **742**, 30 (2011). doi:10.1088/0004-637X/742/1/30

7. D. J. McComas, F. Allegrini, P. Bochsler, M. Bzowski, E. R. Christian, G. B. Crew, R. DeMajistre, H. Fahr, H. Fichtner, P. C. Frisch, H. O. Funsten, S. A. Fuselier, G. Gloeckler, M. Gruntman, J. Heerikhuisen, V. Izmodenov, P. Janzen, P. Knappenberger, S. Krimigis, H. Kucharek, M. Lee, G. Livadiotis, S. Livi, R. J. MacDowall, D. Mitchell, E. Möbius, T. Moore, N. V. Pogorelov, D. Reisenfeld, E. Roelof, L. Saul, N. A. Schwadron, P. W. Valek, R. Vanderspek, P. Wurz, G. P. Zank, Global observations of the interstellar interaction from the Interstellar Boundary Explorer (IBEX). *Science* **326**, 959–962 (2009). doi:10.1126/science.1180906 Medline

8. M. Witte, Kinetic parameters of interstellar neutral helium. *Astron. Astrophys.* **426**, 835–844 (2004). doi:10.1051/0004-6361:20035956

9. C. S. Weller, R. R. Meier, Observations of helium in the interplanetary/interstellar wind - The solar-wake effect. *Astrophys. J.* **193**, 471 (1974). doi:10.1086/153182

10. J. M. Ajello, An interpretation of Mariner 10 helium (584 A) and hydrogen (1216 A) interplanetary emission observations. *Astrophys. J.* **222**, 1068 (1978). doi:10.1086/156224

11. J. M. Ajello, N. Witt, P. W. Blum, Four UV observations of the interstellar wind by Mariner 10. *Astron. Astrophys.* **73**, 260 (1979).

12. C. S. Weller, R. R. Meier, Characteristics of the helium component of the local interstellar medium. *Astrophys. J.* **246**, 386 (1981). doi:10.1086/158936

13. F. Dalaudier, J. L. Bertaux, V. G. Kurt, E. N. Mironova, Characteristics of interstellar helium observed with Prognoz 6 58.4-nm photometers. *Astron. Astrophys.* **134**, 171 (1984).

14. J. Vallerga, R. Lallement, M. Lemoine, F. Dalaudier, D. McMullin, EUVE observations of the helium glow: Interstellar and solar parameters. *Astron. Astrophys.* **426**, 855–865 (2004). doi:10.1051/0004-6361:20035887

15. G. Gloeckler, E. Möbius, J. Geiss, M. Bzowski, S. Chalov, H. Fahr, D. R. McMullin, H. Noda, M. Oka, D. Rucinski, R. Skoug, T. Terasawa, R. von Steiger, A. Yamazaki, T. Zurbuchen, Observations of the helium focusing cone with pickup ions. *Astron. Astrophys.* **426**, 845–854 (2004). doi:10.1051/0004-6361:20035768

16. C. Drews, L. Berger, R. F. Wimmer-Schweingruber, P. Bochsler, A. B. Galvin, B. Klecker, E. Möbius, Inflow direction of interstellar neutrals deduced from pickup ion measurements at 1 AU. *Space Phy.* **117**, 9106 (2012). doi:10.1029/2012JA017746

17. D. J. Gershman, G. Gloeckler, J. A. Gilbert, J. M. Raines, L. A. Fisk, S. C. Solomon, E. C. Stone, T. H. Zurbuchen, Observations of interstellar helium pickup ions in the inner heliosphere. *J. Geophys. Res. Space Phys.* **118**, 1389–1402 (2013). doi:10.1002/jgra.50227

18. E. Möbius, M. Bzowski, S. Chalov, H.-J. Fahr, G. Gloeckler, V. Izmodenov, R. Kallenbach, R. Lallement, D. McMullin, H. Noda, M. Oka, A. Pauluhn, J. Raymond, D. Rucinski, R. Skoug, T. Terasawa, W. Thompson, J. Vallerga, R. von Steiger, M. Witte, Synopsis of the interstellar He parameters from combined neutral gas, pickup ion and UV scattering observations and related consequences. *Astron. Astrophys.* **426**, 897–907 (2004). doi:10.1051/0004-6361:20035834

19. G. P. Zank, J. Heerikhuisen, B. E. Wood, N. V. Pogorelov, E. Zirnstein, D. J. McComas, Heliospheric structure: The bow wave and the hydrogen wall. *Astrophys. J.* **763**, 20 (2013). doi:10.1088/0004-637X/763/1/20

20. H. Nakagawa, M. Bzowski, A. Yamazaki, H. Fukunishi, S. Watanabe, Y. Takahashi, M. Taguchi, I. Yoshikawa, K. Shiomi, M. Nakamura, UV optical measurements of the Nozomi spacecraft interpreted with a two-component LIC-flow model. *Astron. Astrophys.* **491**, 29–41 (2008). doi:10.1051/0004-6361:20079241

21. H. J. Fahr, H. U. Nass, D. Rucinski, *Astron. Astrophys.* **142**, 476 (1985).

22. M. Gruntman, *J. Geophys. Res. Space Phys.* **118**, 1366–1378 (2013).

23. M. A. Lee, H. Kucharek, E. Möbius, X. Wu, M. Bzowski, D. McComas, An analytical model of interstellar gas in the heliosphere tailored to Interstellar Boundary Explorer observations. *Astrophys. J. Suppl.* **198**, 10 (2012). doi:10.1088/0067-0049/198/2/10

24. H.-R. Müller, J. H. Cohen, in *American Institute of Physics Conference Proceedings*, J. Heerikhuisen, G. Li, N. Pogorelov, G. Zank, Eds. (AIP Publishing, College Park, MD, 2012), vol. 1436, pp. 233–238.

25. D. R. McMullin, M. Bzowski, E. Möbius, A. Pauluhn, R. Skoug, W. T. Thompson, M. Witte, R. von Steiger, D. Rucinski, D. Judge, M. Banaszkiewicz, R. Lallement, Heliospheric conditions that affect the interstellar gas inside the heliosphere. *Astron. Astrophys.* **426**, 885–895 (2004). doi:10.1051/0004-6361:20047147

26. M. Bzowski *et al*., in *Cross-Calibration of Past and Present Far UV Spectra of Solar System Objects and the Heliosphere*, *SSI Scientific Report Series 13*, M. S. R. M. Bonnet, E. Qumerais, Eds. (Springer, New York, 2013), pp. 67–138.

27. R. Lallement, J. C. Raymond, J. Vallerga, M. Lemoine, F. Dalaudier, J. L. Bertaux, Modeling the interstellar-interplanetary helium 58.4 nm resonance glow: Towards a reconciliation with particle measurements. *Astron. Astrophys.* **426**, 875–884 (2004). doi:10.1051/0004-6361:20035929

28. R. Lallement *et al*., The interstellar H flow: Updated analysis of SOHO/SWAN data. *Twelfth Int. Solar Wind Conf.* **58**, 951 (2010).

29. P. C. Frisch, M. Bzowski, E. Grün, V. Izmodenov, H. Krüger, J. L. Linsky, D. J. McComas, E. Möbius, S. Redfield, N. Schwadron, R. Shelton, J. D. Slavin, B. E. Wood, The galactic environment of the Sun: Interstellar material inside and outside of the heliosphere. *Space Sci. Rev.* **146**, 235–273 (2009). doi:10.1007/s11214-009-9502-0

30. P. C. Frisch, J. M. Dorschner, J. Geiss, J. M. Greenberg, E. Grun, M. Landgraf, P. Hoppe, A. P. Jones, W. Kratschmer, T. J. Linde, G. E. Morfill, W. Reach, J. D. Slavin, J. Svestka, A. N. Witt, G. P. Zank, Dust in the local interstellar wind. *Astrophys. J.* **525**, 492–516 (1999). doi:10.1086/307869

31. H. Kimura, I. Mann, E. K. Jessberger, Elemental abundances and mass densities of dust and gas in the local interstellar cloud. *Astrophys. J.* **582**, 846–858 (2003). doi:10.1086/344691

32. S. Belheouane *et al*., Detection of interstellar dust with STEREO/WAVES at 1 AU. *Sol. Phys.* **281**, 501 (2012).

33. H. Krüger, V. Dikarev, B. Anweiler, S. F. Dermott, A. L. Graps, E. Grün, B. A. Gustafson, D. P. Hamilton, M. S. Hanner, M. Horányi, J. Kissel, D. Linkert, G. Linkert, I. Mann, J. A. M. McDonnell, G. E. Morfill, C. Polanskey, G. Schwehm, R. Srama, Three years of Ulysses dust data: 2005 to 2007. *Planet. Space Sci.* **58**, 951–964 (2010). doi:10.1016/j.pss.2009.11.002

34. G. Hebrard *et al*., Ultraviolet observations of Sirius A and Sirius B with HST-GHRS. *Astron. Astrophys.* **350**, 643 (1999).

35. J. D. Slavin, P. C. Frisch, The ionization of nearby interstellar gas. *Astrophys. J.* **565**, 364–379 (2002). doi:10.1086/324495

36. P. C. Frisch, L. Grodnicki, D. E. Welty, The velocity distribution of the nearest interstellar gas. *Astrophys. J.* **574**, 834–846 (2002). doi:10.1086/341001

37. R. Lallement, P. Bertin, R. Ferlet, A. Vidal-Madjar, J. L. Bertaux, GHRS observations of Sirius-A. *Astron. Astrophys.* **286**, 898 (1994).

38. W. E. Deming, *Statistical Adjustment of Data* (Dover, New York, 1964).

39. G. Livadiotis, Approach to general methods for fitting and their sensitivity. *Physica A* **375**, 518–536 (2007). doi:10.1016/j.physa.2006.09.027